Electronic Supplementary Information (ESI)

Graphene Stabilized Ultra-small-sized CuNi Nanocomposite with High Activity and Recyclability toward Catalysing the Reduction of Aromatic Nitro-Compounds

Hao Fang, Ming Wen,* Hanxing Chen and Qingsheng Wu

Department of Chemistry, State Key Laboratory of Pollution Control and Resource Reuse, Tongji University, 1239 Siping Road, Shanghai 200092, China.

E-mail: m_wen@tongji.edu.cn; Fax: (+) 86-21-65981097

Table S1. Component molar ratios of as-prepared CuNi alloys NPs.

CuNi alloys	Atom percentages (%)	
	Cu	Ni
$Cu_{20}Ni_{80}$	20.4	79.6
$Cu_{40}Ni_{60}$	41.0	59.0
$Cu_{50}Ni_{50}$	49.6	50.4
$Cu_{58}Ni_{42}$	57.5	42.5
$Cu_{59}Ni_{41}$	59.2	40.8
$Cu_{60}Ni_{40}$	39.3	40.7
$Cu_{61}Ni_{39}$	61.4	38.6
$Cu_{62}Ni_{38}$	62.9	37.1
$Cu_{63}Ni_{37}$	62.6	37.4
$Cu_{64}Ni_{36}$	63.7	36.3
$Cu_{80}Ni_{20}$	79.2	20.8

In order to investigate the best catalytic acitivity vs CuNi alloy ratios, a series of CuNi alloy NPs of different ratios were synthsized. First of all, it is necessary to determine if the real ratios were agreed with the target ratios. The component ratios of samples were determined by inductively coupled plasma (ICP), and the results were summarized in Table S1. It can be concluded from the table that the determined actual ratios were consistent with the initial target ratios of Cu to Ni, it suggests that the metal precursors were reduced completely and formed alloy NPs.

Table S2. Reaction rate constants in different recycles of graphene/CuNi nanocomposite or CuNi alloy NPs as catalysts.

No. of Recycles	Rate constants k (s^{-1})	
	nanocomposite	CuNi alloy NPs
1	0.0806	0.0202
2	0.0977	0.0185
3	0.1064	0.0228
4	0.1039	0.0140
5	0.1011	0.0115
6	0.1004	0.0019
7	0.1138	
8	0.1195	
9	0.1306	
10	0.1234	
11	0.1369	
12	0.1293	
13	0.1048	
14	0.1270	
15	0.1173	
16	0.1288	
17	0.1021	
18	0.0997	
19	0.1286	
20	0.0961	
21	0.1284	
22	0.1025	
23	0.1109	
24	0.1347	
25	0.1083	

Table S2 summaries rate constants of different recycles for graphene/CuNi nanocomposite and CuNi alloys NPs. The catalytic activity of graphene/CuNi could keep over 25 times for reduction of p-nitrophenol. The reaction rate constants were only slightly changed during the 25 recycles. As contrast, the rate constants of CuNi NPs dropped drastically after the 6th recycle, because the CuNi NPs merged together during the catalysis process. This lead to the surface area decrease of CuNi NPs, therefore, reaction rate constants dropped obviously. But for the nanocomposite, graphene provides a strong support to prevent the NPs from agglomerating together. So the nanocomposite have excellent activity and stability in the catalytic reduction of p-nitrophenol than the CuNi NPs without graphene support.
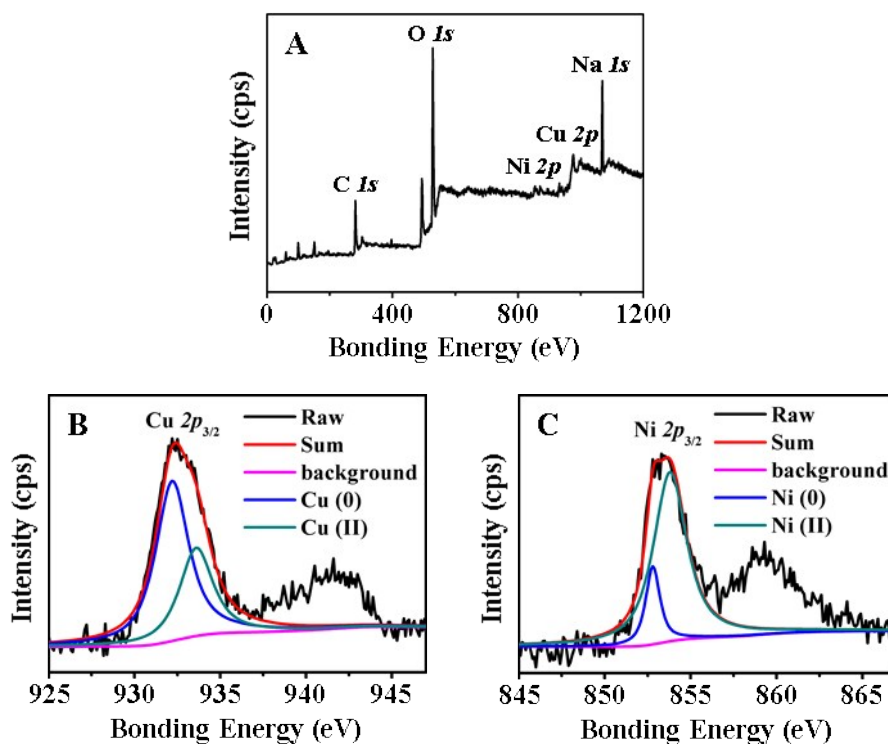
Fig. S1. XPS analysis of the graphene/CuNi nanocomposite after 25 catalysis recycles: (A) full spectrum of the catalyst after 25 catalysis recycles, (B) detailed spectrum of Cu after catalysis, (C) detailed spectrum of Ni after catalysis.

Fig. S1A exhibited the XPS full spectra of the graphene/CuNi nanocomposite catalyst after 25 catalytic recycles. C 1s, O 1s, Cu 2p, Ni 2p peaks corresponding to the component elements were detected in the full spectra. Besides, Na 1s peak of binding energy of 1069 eV was detected, showing redidues of Na ions exist on the catalyst surface. Fig. S1B and C show the the binding energy of Cu 2p3/2 and Ni 2p3/2 spectra from recycled catalyst. In Fig. S1B, the binding energy of 932.5 eV was attributed to Cu(0) metal. In addition, the characteristic peak of 933.8 eV which related to the Cu(II) were also detected. Hence, it is concluded that CuO exist on the surface of the catalyst after 25 recycles. In Fig. S1C, the peak at ~852.6 eV was observed, which was indexed to the Ni(0). Besides, peak related to Ni(II) were also detected with binding energy of 854 eV. It revealed that the Ni was partially oxided to NiO.
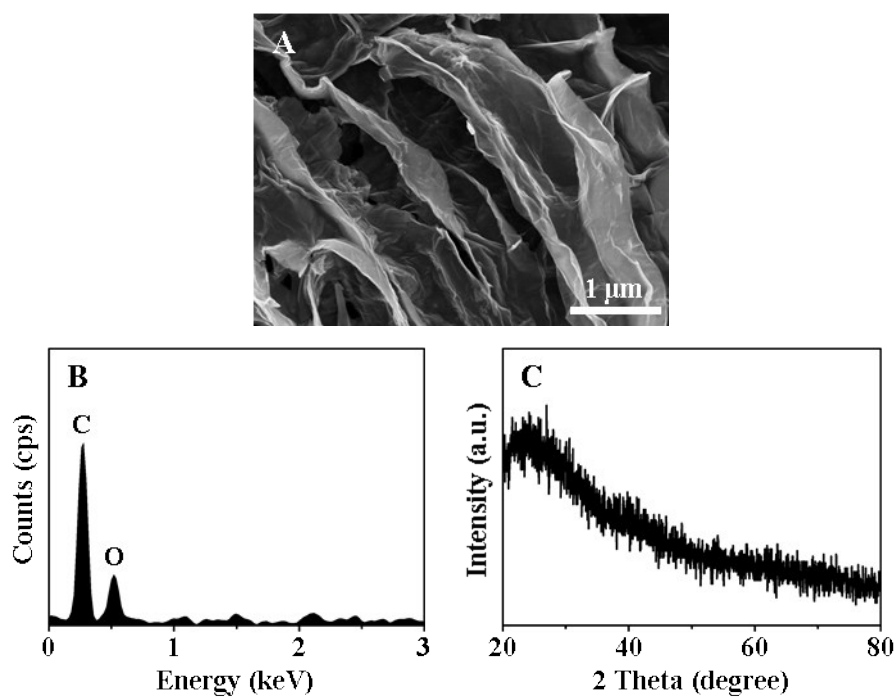
Fig. S2. (A) SEM image, (B) EDS spectrum, (C) XRD pattern of reduced graphene oxide.

Fig. S2 presents the characteristic information of as-prepared reduced graphene oxide. The SEM image shows wrinkles on it (Fig. S2A). In Fig. S2B, the EDS spectrum shows the element of C and O were detected. XRD pattern in Fig. S2C shows the characteristic peak of reduced graphene oxide at about 25 degree.
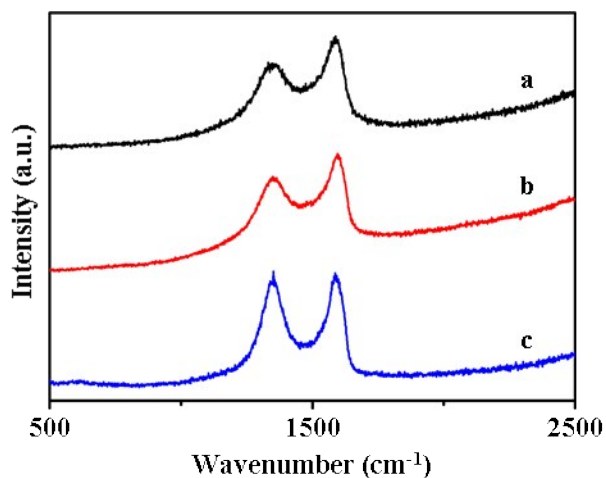
Fig. S3. Raman spectra of (a) graphene/CuNi nanocomposite; (b) reduced graphene oxide; (c) graphene oxide.

In order to characterize the degree of restoration of the carbon sp^2 structues after the reduction, Raman spectra were carried out to investigate the changes between the graphene oxide and its reduction resultant. The curves in Fig. S3 presented the Raman spectra of graphene/CuNi nanocomposite (a), reduced graphene oxide (b) and graphene oxide (c). Curves (a) and (b) have similar intensity ratio of peak D to peak G, but differ from that of curve (c). The ratio of peak D to G altered distinctly after the reduction, from the value of 1.074 to 0.724, revealed obvious changes in the carbon structure have taken place. The lower value of peak D to G indicates the sp^2 hybridized structure of graphene obtained effective restoration during the reduction process, and the oxygen groups have been removed effectively in the nanocomposite, it also conformed with the fabrication mechanism of the graphene/CuNi nanocomposite.
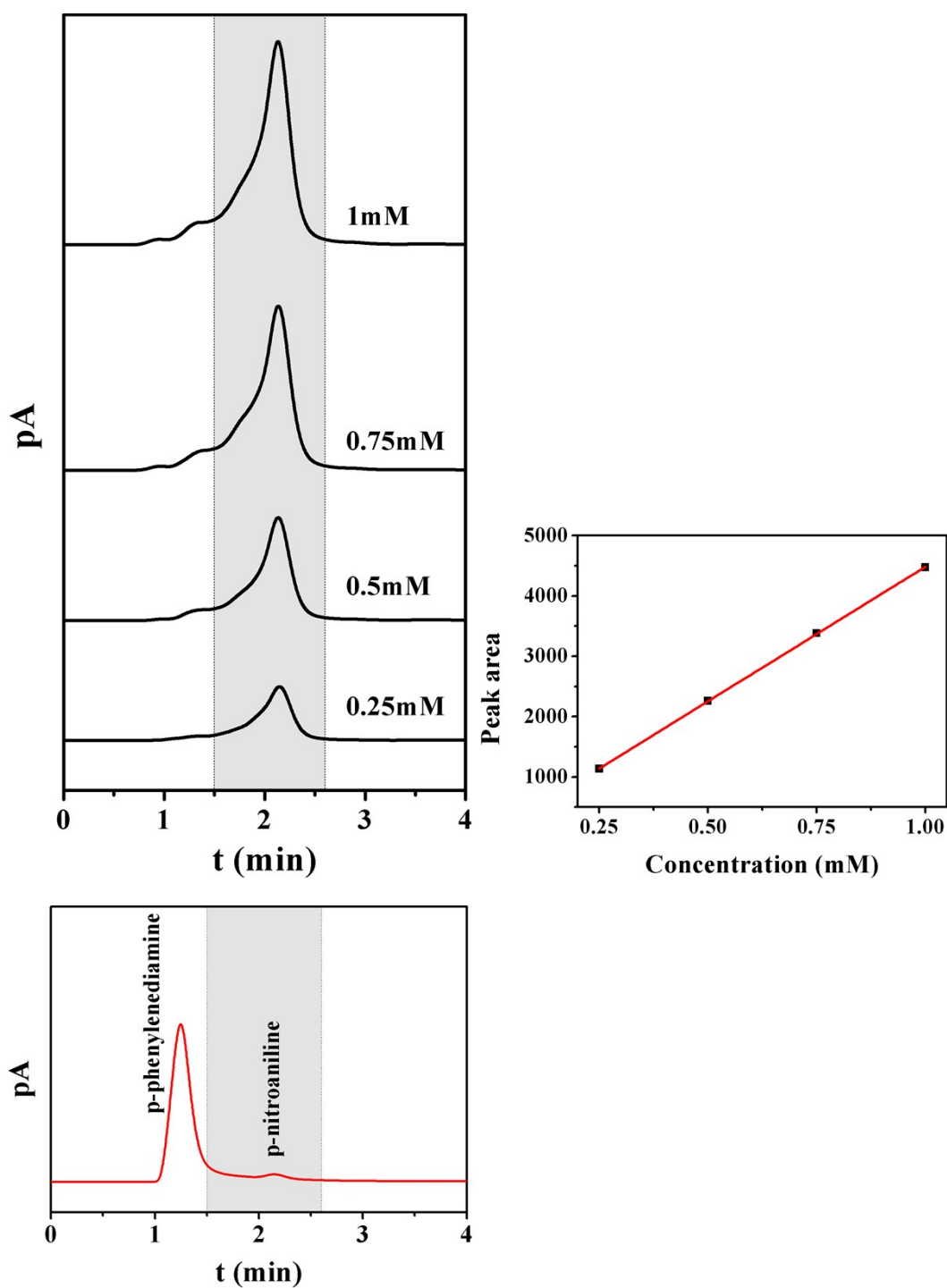
Fig. S4-1. Chromatograms of p-nitroaniline (peaks in black) or p-phenylenediamine (peaks in red) and fitted standard curve.

We prepared four standard solutions in different concentrations, and further obtained four standard chromatograms (in black). The linear relation between peak areas and concentrations was fitted and characterized by the *regression equation* as below. The accuracy of this equation can be quantified by *correlation coefficient*, which is highly

reliable if higher than 0.99. From the chromatogram of catalysis reaction (in red), residue amount of aromatic nitro-compounds can be obtained through peak area (in grey shadow zone). In virtue of regression equation, the concentration and conversion rate of aromatic nitro-compounds can be readily figured out.

Regression equation: $A=4452.90503C+27.99927$ (A stands for the peak area of aromatic nitro-compounds, while C stands for the concentration of corresponding solution. The following equations are the same.)

Correlation coefficient: R=0.9997

Conversion (%): 98.74

Selectivity (%): >99.99 (no detectable by-product)
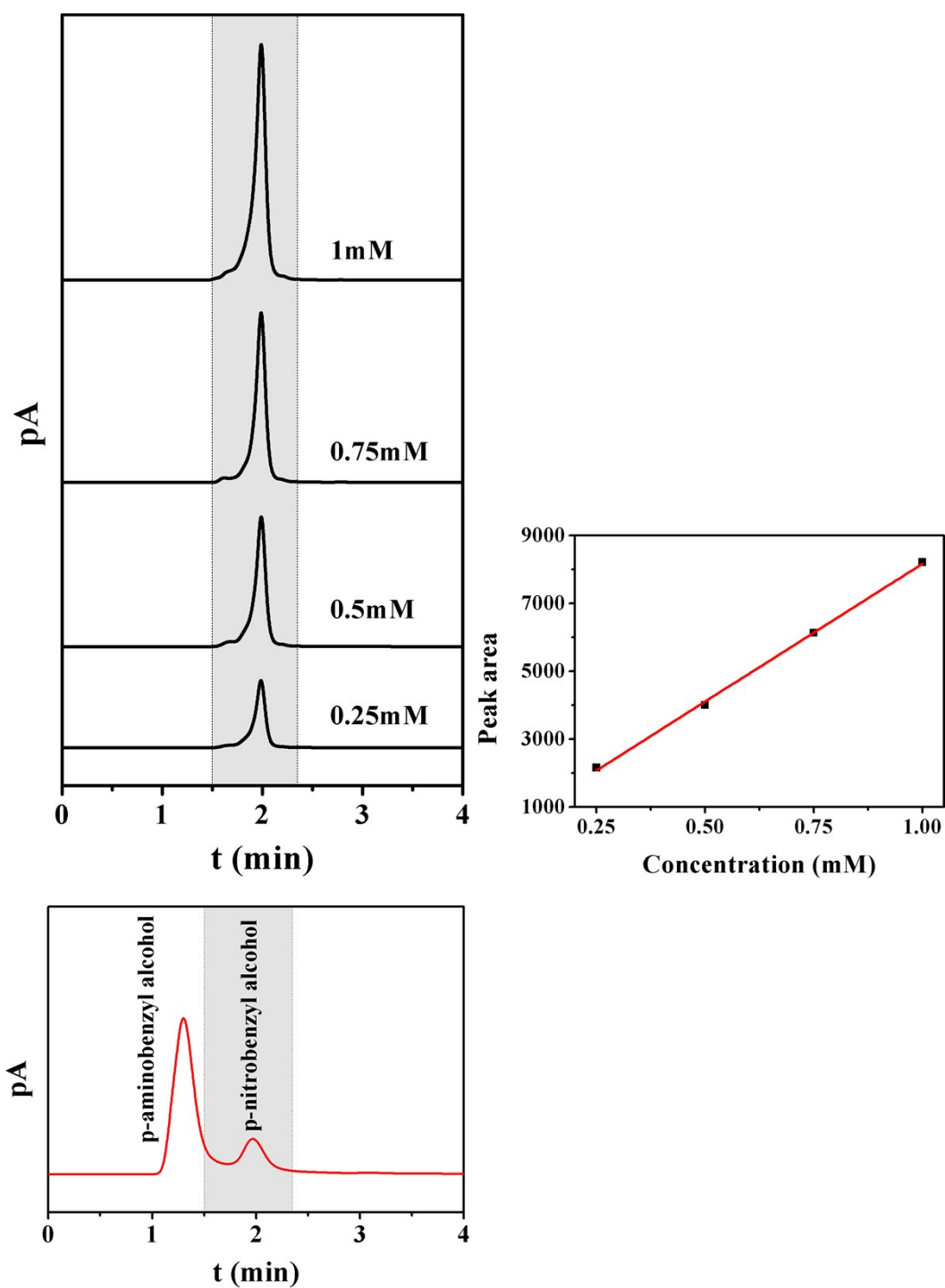
Fig. S4-2. Chromatograms of p-nitrobenzyl alcohol (peaks in black) or p-aminobenzyl alcohol (peaks in red) and fitted standard curve.

Regression equation: A=8111.61776C+54.78711

Correlation coefficient: R=0.99954

Conversion (%): 77.59

Selectivity (%): >99.99 (no detectable by-product)
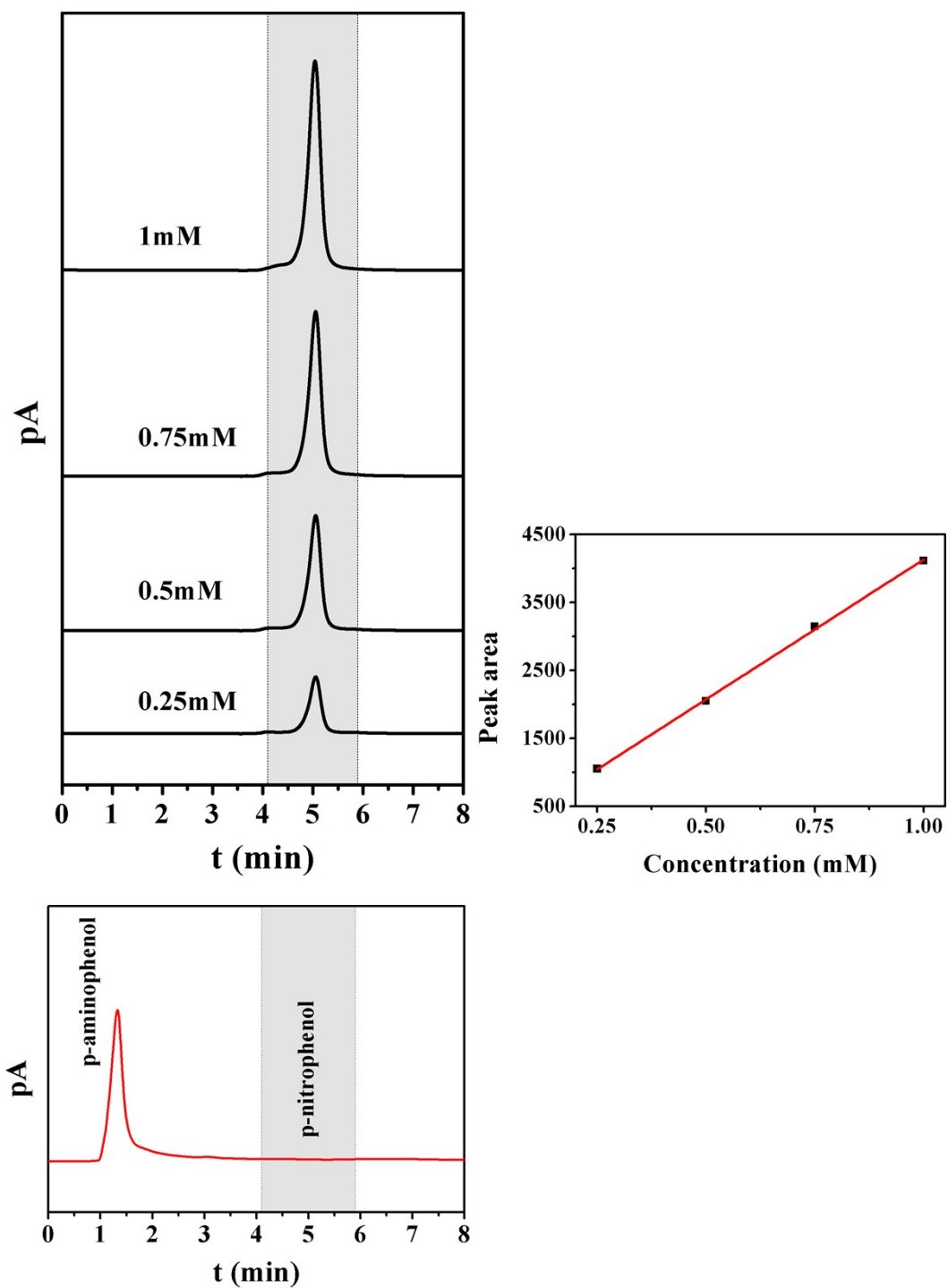
Fig. S4-3. Chromatograms of p-nitrophenol (peaks in black) or p-aminophenol (peaks in red) and fitted standard curve.

Regression equation: A=4111.91994C+19.23004

Correlation coefficient: R=0.99973

Conversion (%): >99.99 (no detectable residue)

Selectivity (%): >99.99 (no detectable by-product)
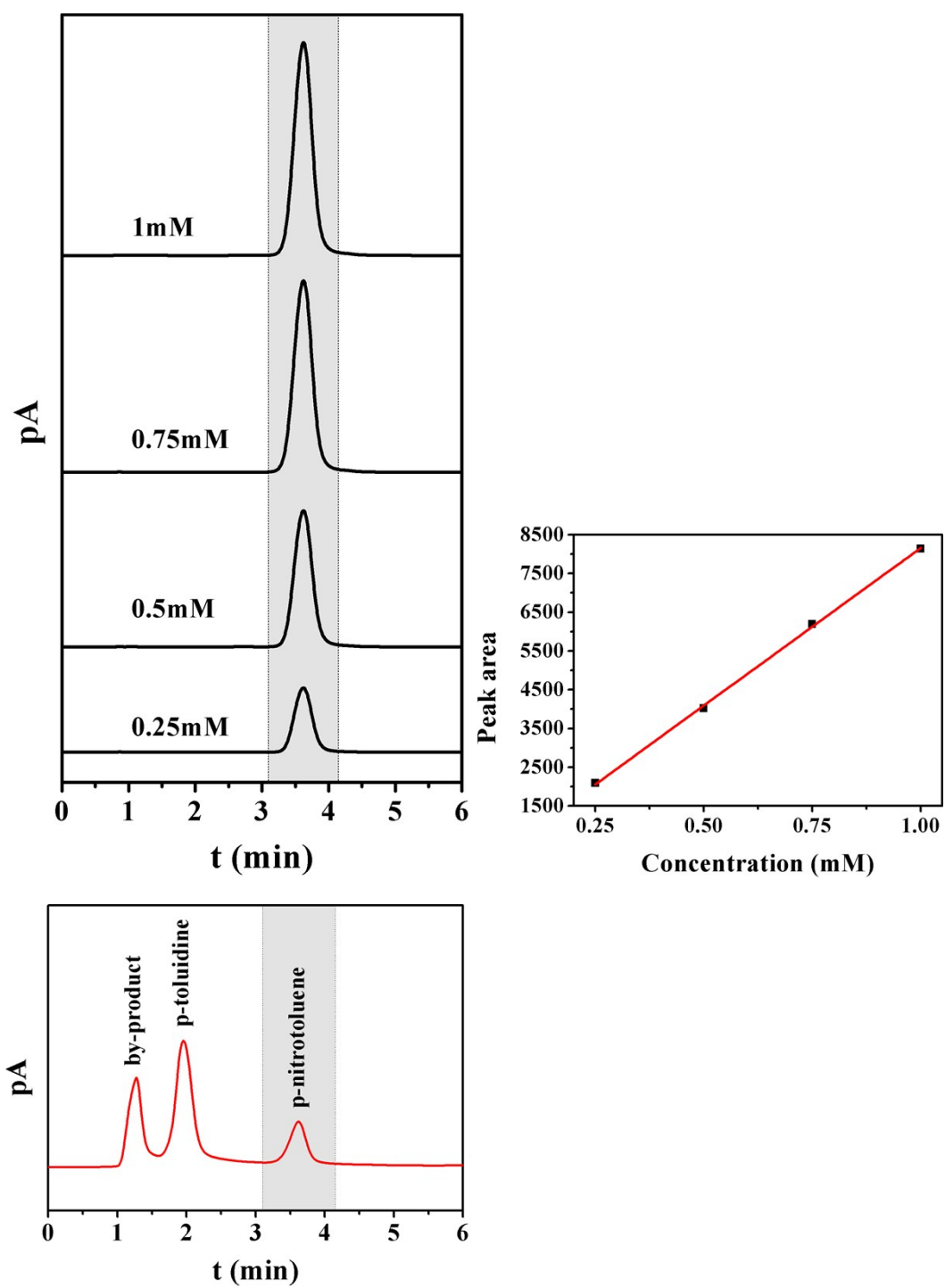
Fig. S4-4. Chromatograms of p-nitrotoluene (peaks in black) or p-toluidine (peaks in red) and fitted standard curve.

Regression equation: A=8129.97901C+28.85595

Correlation coefficient: R=0.99964

Conversion (%): 79.53

Selectivity (%): 64.67
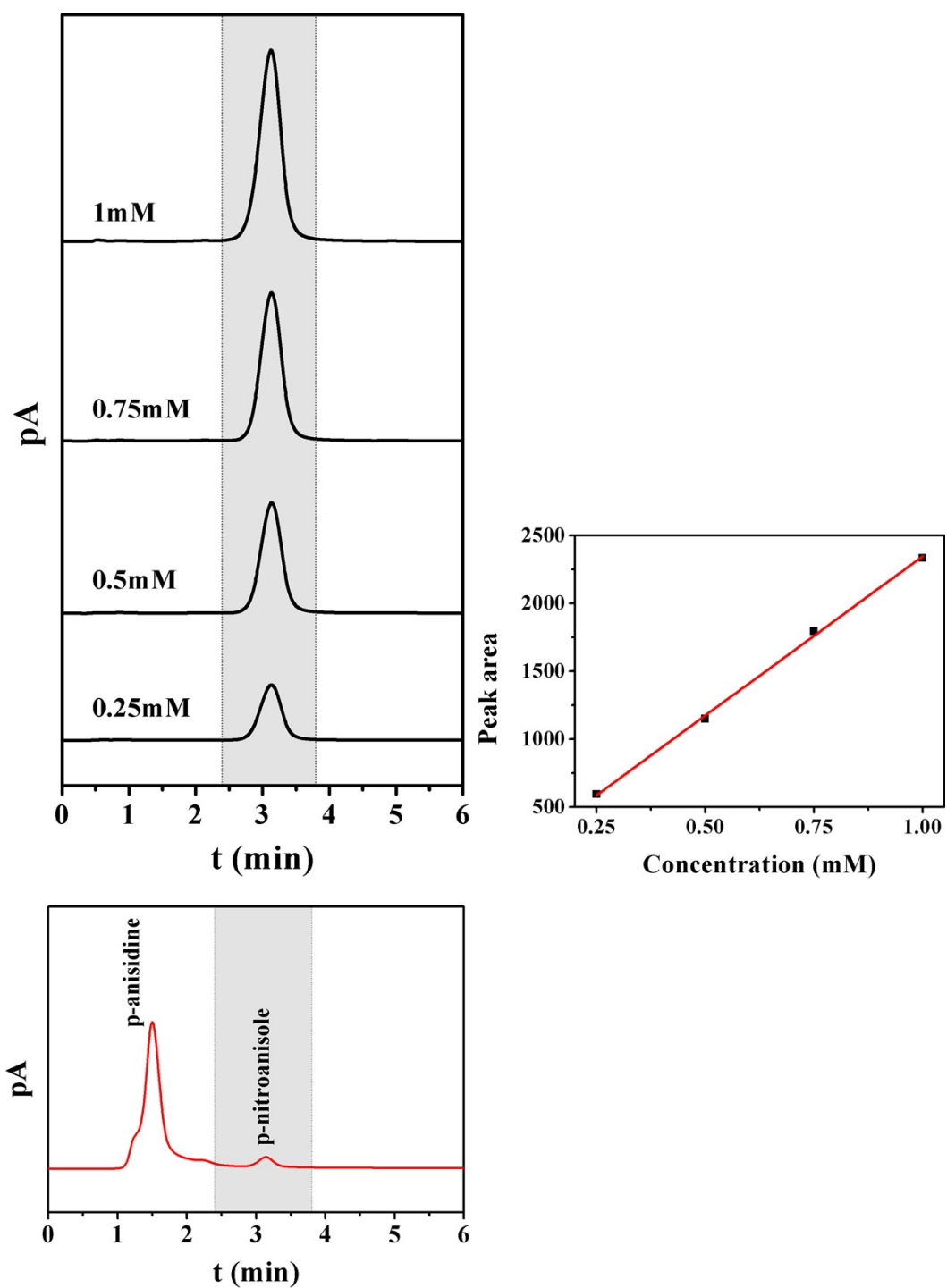
Fig. S4-5. Chromatograms of p-nitroanisole (peaks in black) or p-anisidine (peaks in red) and fitted standard curve.

Regression equation: A=2344.0458C+2.89483

Correlation coefficient: R=0.9941

Conversion (%): 95.47

Selectivity (%): >99.99 (no detectable by-product)
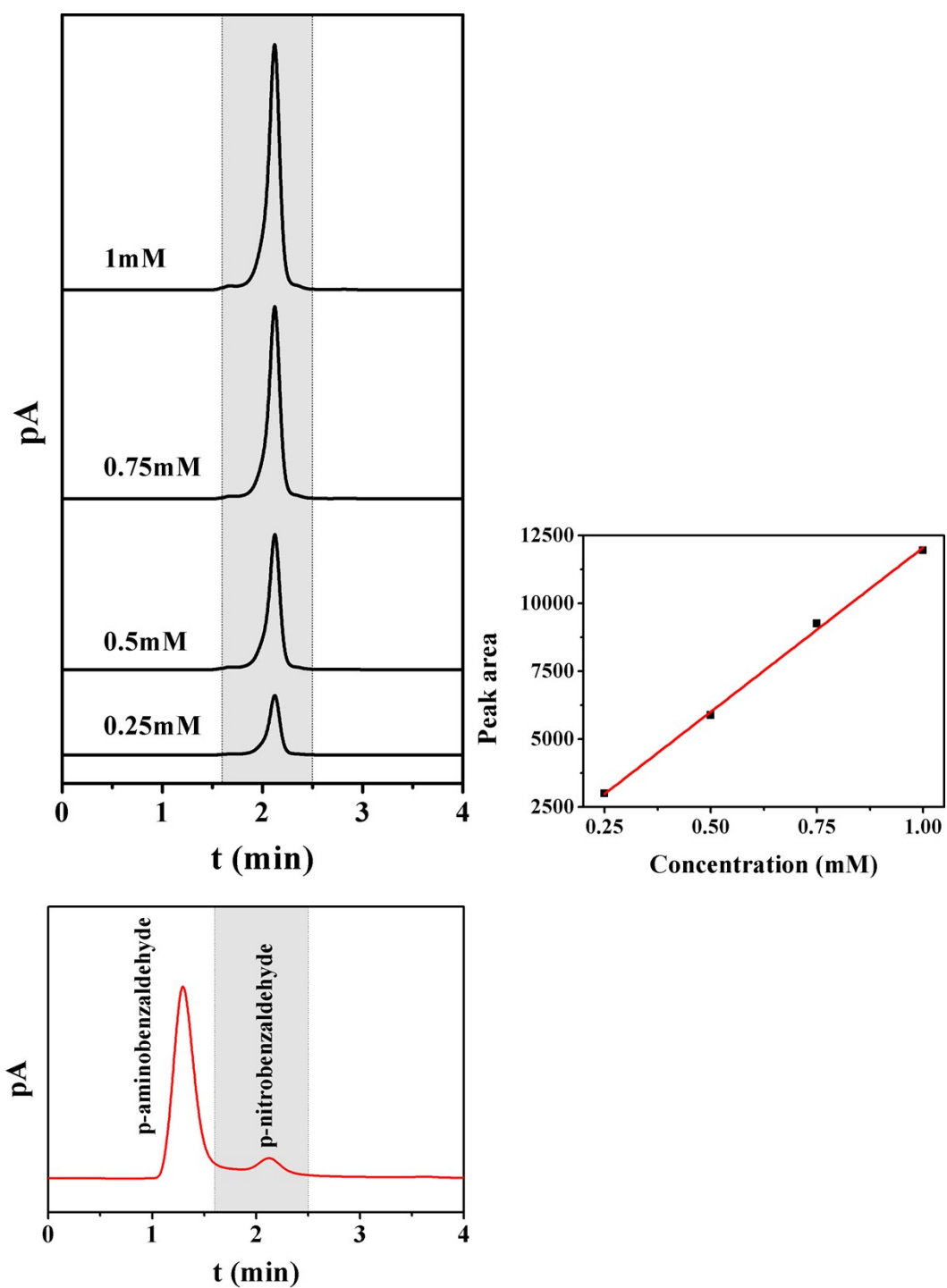
Fig. S4-6. Chromatograms of p-nitrobenzaldehyde (peaks in black) or p-aminobenzaldehyde (peaks in red) and fitted standard curve.

Regression equation: A=12089.67584C-33.65665

Correlation coefficient: R=0.9961

Conversion (%): 86.56

Selectivity (%): >99.99 (no detectable by-product)
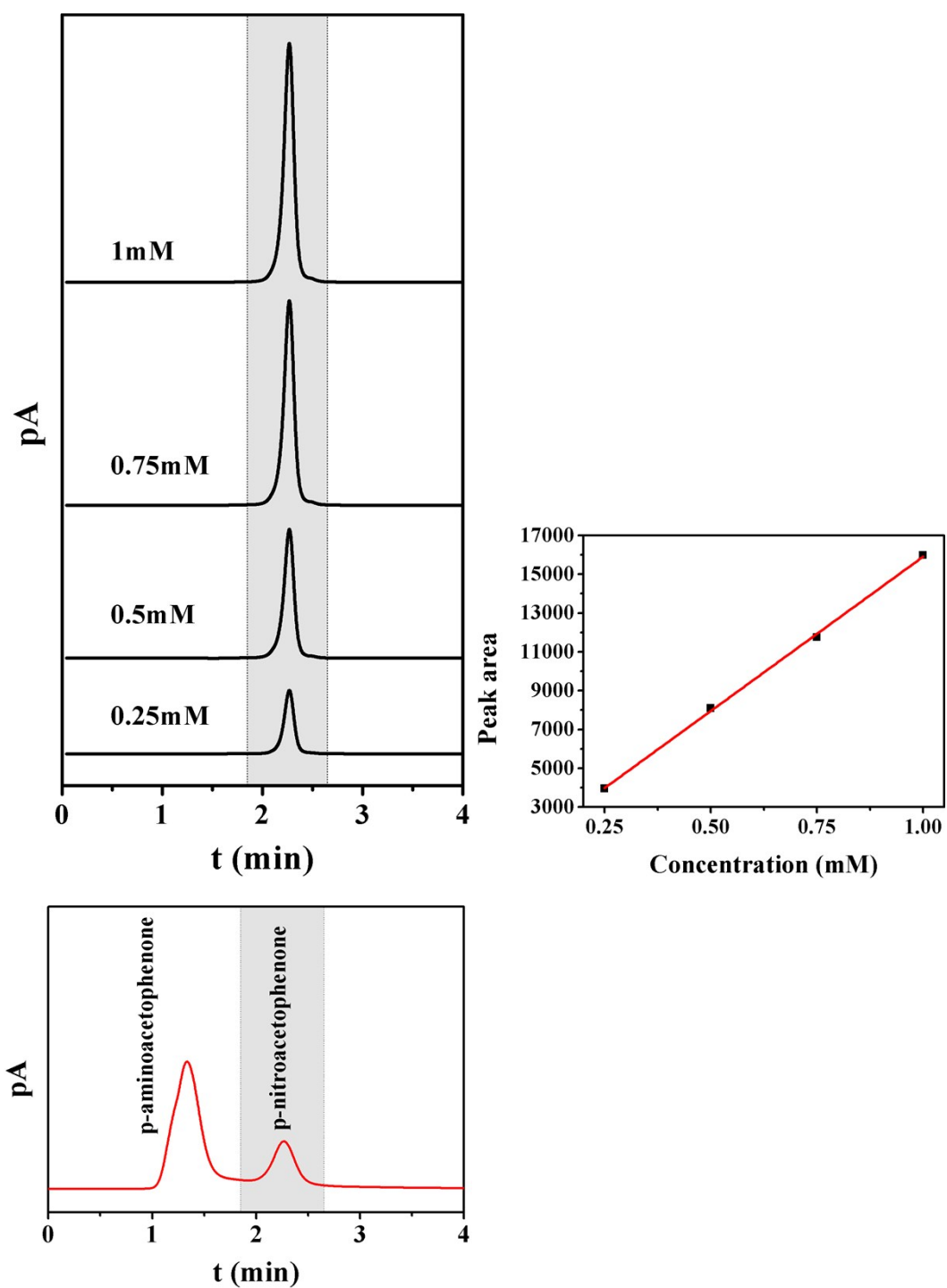
Fig. S4-7. Chromatograms of p-nitroacetophenone (peaks in black) or p-aminoacetophenone (peaks in red) and fitted standard curve.

Regression equation: $A=15897.74973C+9.35102$

Correlation coefficient: $R=0.99946$

Conversion (%): 72.54

Selectivity (%): >99.99 (no detectable by-product)
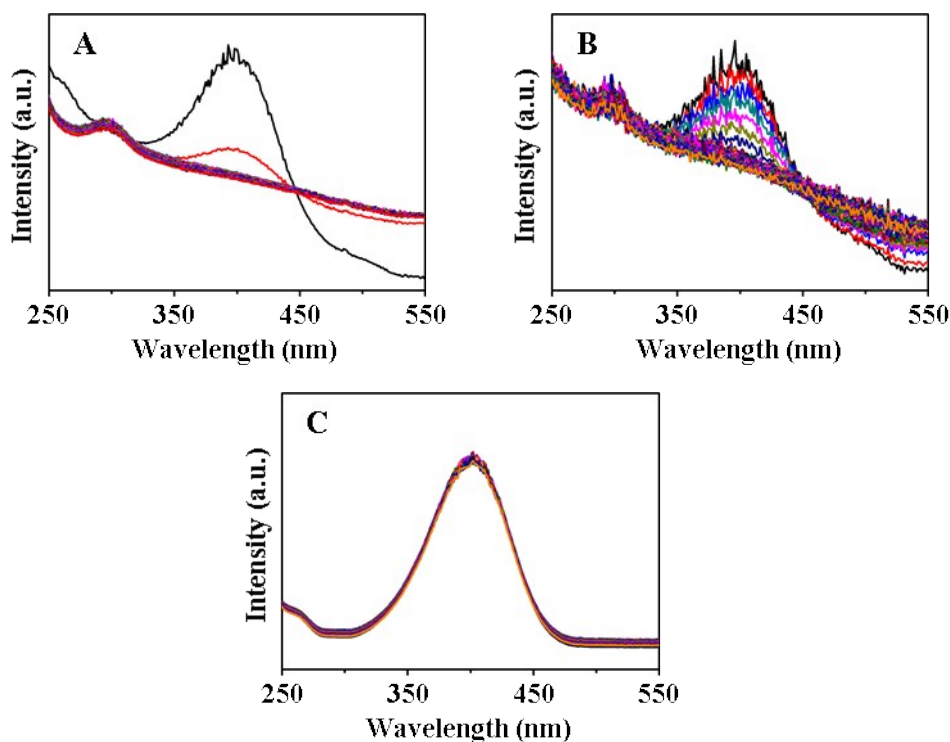
Fig. S5. UV-Vis adsorption spectra using different catalysts: (A) graphene/$Cu_{61}Ni_{39}$ nanocomposite; (B) $Cu_{61}Ni_{39}$ alloy NPs; (C) graphene.

Fig. S5 exhibits the overlapped UV-Vis adsorption spectra recorded at different reaction time of the three catalysts. The major peak at 400 nm indexed to p-nitrophenolate ion, and the minor peak of 300 nm is characteristic peak of p-aminophenol. In Fig. S5A, the peak of p-nitrophenol decreased immediately, and the reation finished in seconds. Meanwhile, the peak of 300 nm increased. But as the contrast shown in Fig. S5B, the CuNi alloy NPs shows much lower rate than the nanocomposite. The peak at 400 nm decreased completely in a longer time than the nanocomposite. While graphene exhibits no activity in the catalysis reaction. The concentration of p-nitrophenol is constant without any decrease and showed as a series of overlapped spectra. It demonstrates that the graphene/CuNi nanocomposite have the best performance than their components. Although the activity is from the CuNi alloy NPs, but for the well distribution of the NPs on the graphene support, the nanocomposite obtained larger suface area than the CuNi NPs, achieved better catalytic performance.
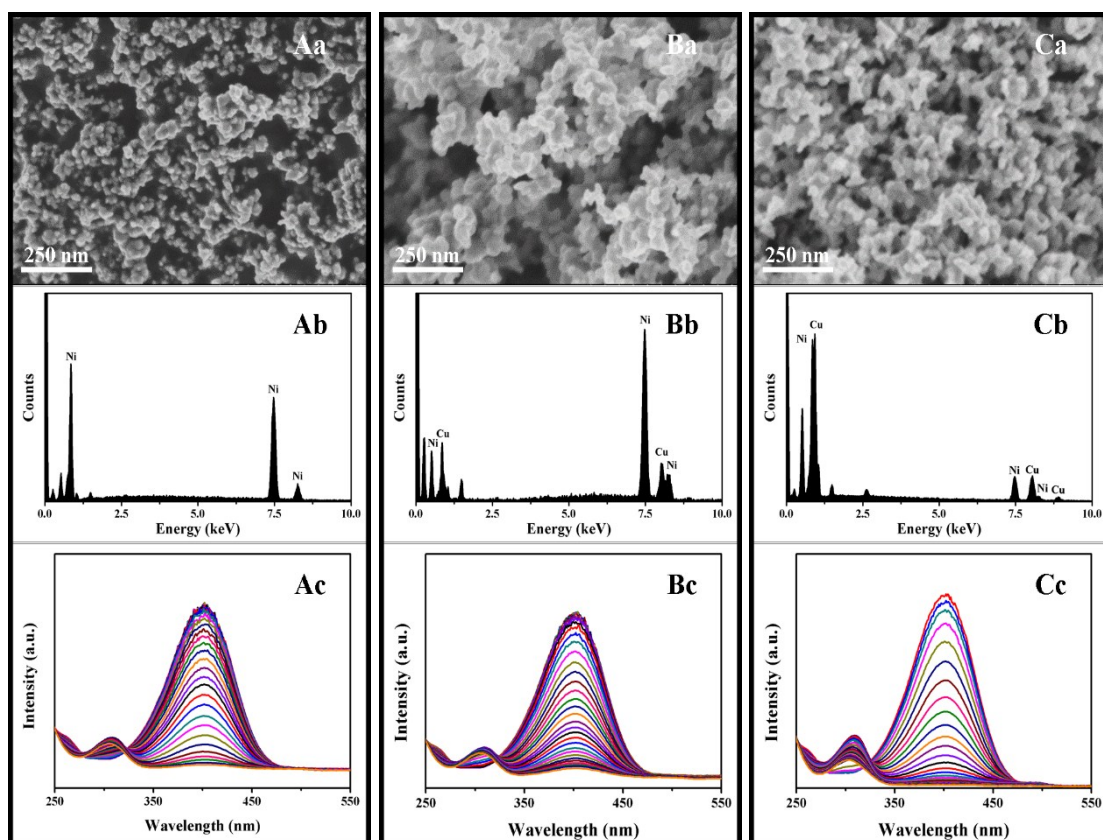
Fig. S6-1. (a) SEM images, (b) EDS analysis and (c) UV-Vis spectra of CuNi alloy NPs of different compositions: (A) Cu; (B) $Cu_{80}Ni_{20}$; (C) $Cu_{60}Ni_{40}$.
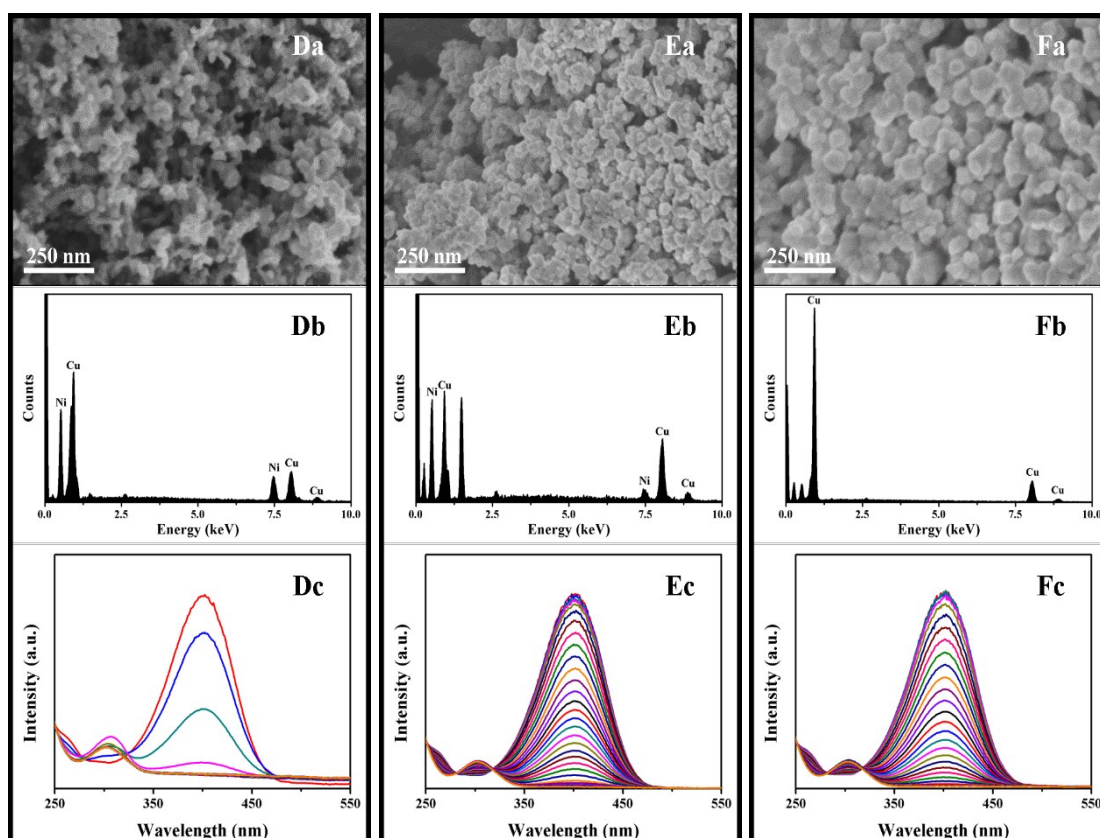
Fig. S6-2. (a) SEM images, (b) EDS analysis and (c) UV-Vis spectra of CuNi alloy NPs of different compositions: (D) $Cu_{40}Ni_{20}$; (E) $Cu_{20}Ni_{80}$; (F) Ni.

The catalytic activities toward the reduction of p-nitrophenol were investigated using CuNi alloy NPs of different composition, shown in Fig. S6-1 and S6-2. It can be seen from Fig. S6 that the catalytic reduction rates related to the Cu to Ni ratios and increased with the Cu component content increase. The activity reach the highest point at about $Cu_{60}Ni_{40}$, but further increase of Cu content lead to the decrease of the catalytic activity. It revealed the alloy have better performance than pure Cu or Ni, appropriate ratio can lead to the optimal catalytic performance. So further detailed optimizing is carried out.
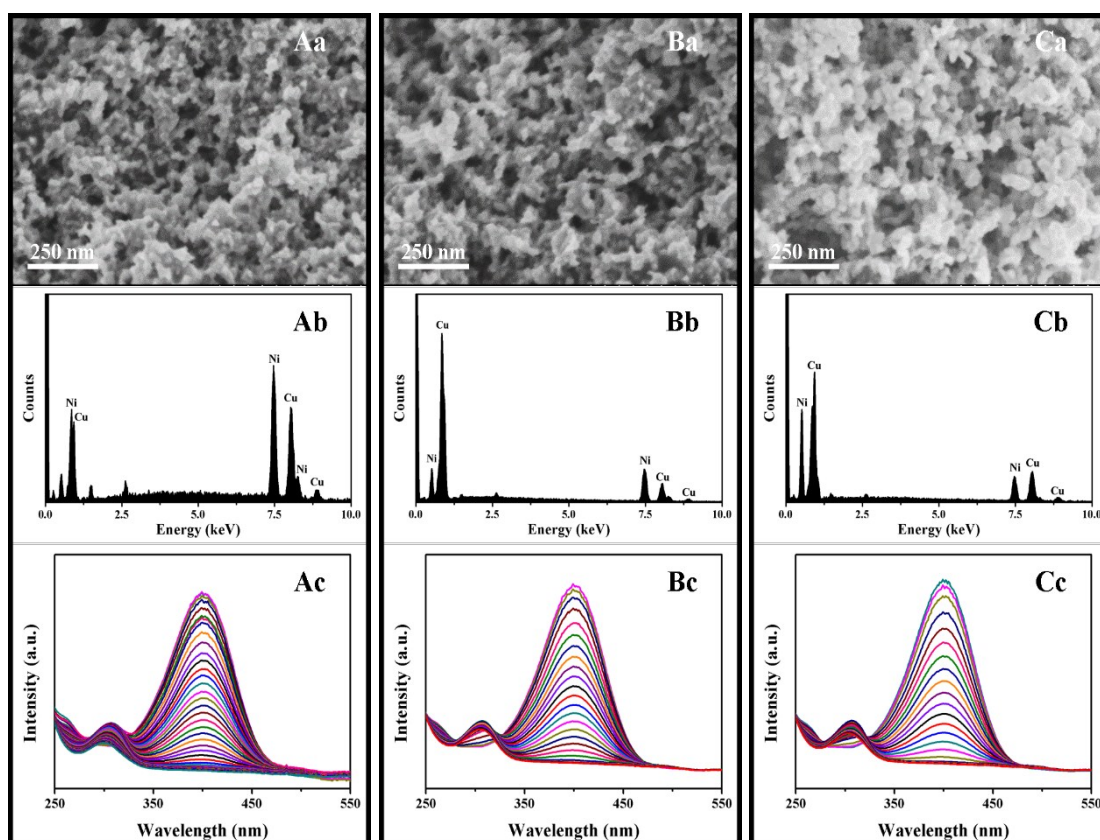
Fig. S7-1. (a) SEM images, (b) EDS analysis and (c) UV-Vis spectra of CuNi alloy NPs of different compositions: (A) $Cu_{58}Ni_{42}$; (B) $Cu_{59}Ni_{41}$; (C) $Cu_{60}Ni_{40}$.
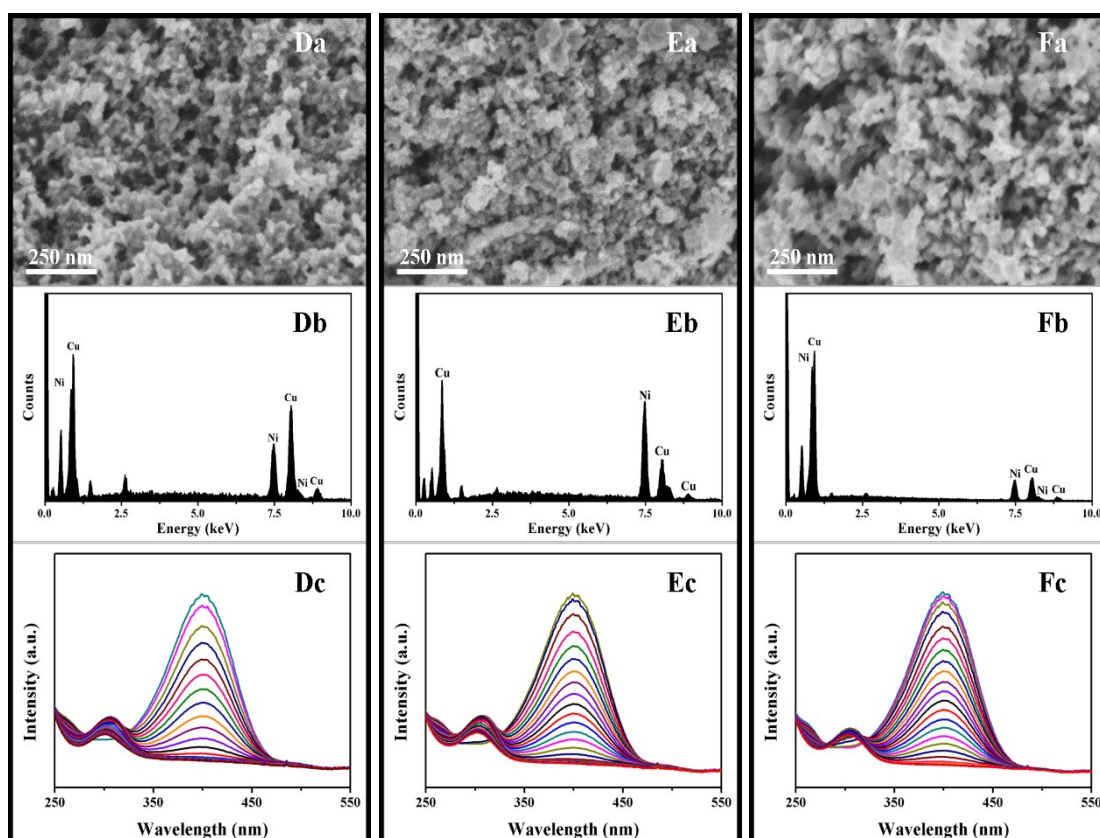
Fig. S7-2. (a) SEM images, (b) EDS analysis and (c) UV-Vis spectra of CuNi alloy NPs of different compositions: (D) $Cu_{61}Ni_{39}$; (E) $Cu_{62}Ni_{38}$; (F) $Cu_{63}Ni_{37}$.

In order to obtain the optimal Cu/Ni ratio to the catalytic reaction, more accurate adjustment of Cu to Ni ratios of $Cu_{58}Ni_{42}$, $Cu_{59}Ni_{41}$, $Cu_{60}Ni_{40}$, $Cu_{61}Ni_{39}$, $Cu_{62}Ni_{38}$ and $Cu_{63}Ni_{37}$ was prepared to investigate the highest catalytic activity. Finally, $Cu_{61}Ni_{39}$ was most active ratio and presents the highest catalytic activity for reducing p-nitrophenol. The reason can be suggested that the nickel atoms of less catalytic activity alloyed into the copper lattice, and seperated the copper atoms of higher activity. When the ratio is $Cu_{61}Ni_{39}$, Cu atoms have the best spacing to fit p-nitrophenol molecule, so the alloy reached optimal performance at this ratio.
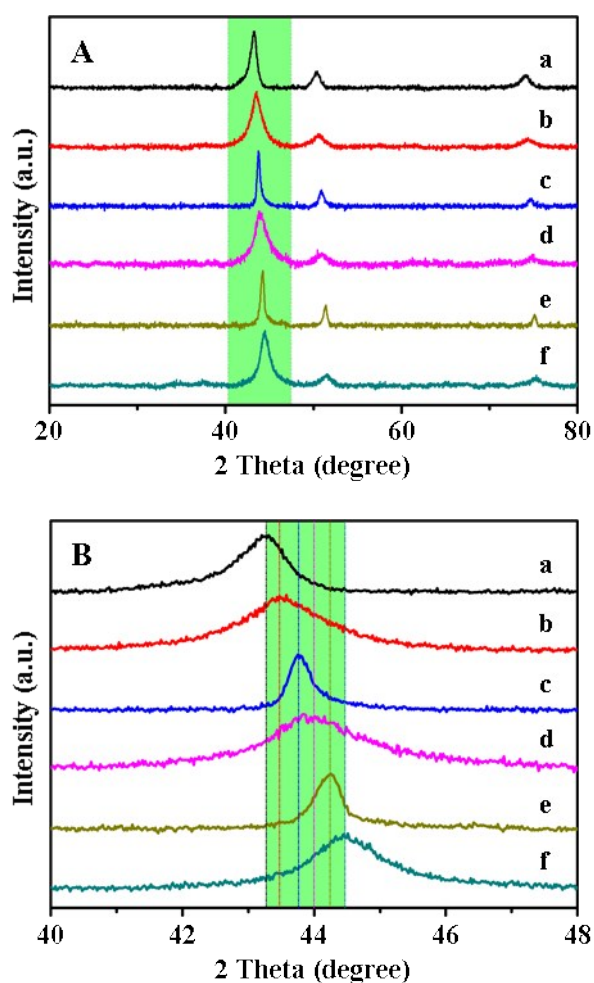
Fig. S8. XRD patterns of CuNi alloy NPs of different ratios of (a) Cu; (b) $Cu_{80}Ni_{20}$; (c) $Cu_{60}Ni_{40}$; (d) $Cu_{40}Ni_{60}$; (e) $Cu_{20}Ni_{80}$, (f) Ni showed in (A) wide range and (B) magnified range of diffraction angles of 40-48 degree.

CuNi alloy NPs of different ratios have similar XRD patterns with continuous shift from pure Cu (a) to pure Ni (f), because they have the same latices. So Cu and Ni can form typical continuous solid solution. In this alloy system, XRD pattern can continuously shift as the component change. From magnified green part in Fig. S8B located at 2θ between 43.3 to 44.5 degree, it is noticeable that the peaks of (111) of CuNi alloy NPs shift slightly to high angle oritation, peak of Cu (111) continuously shifts from 2θ of 43.3 degree to Ni (111) of 44.5 degree. As the ratio of Ni increases, the peak shifts to high angle, suggesting the lattices was gradual substituted by Ni atoms.
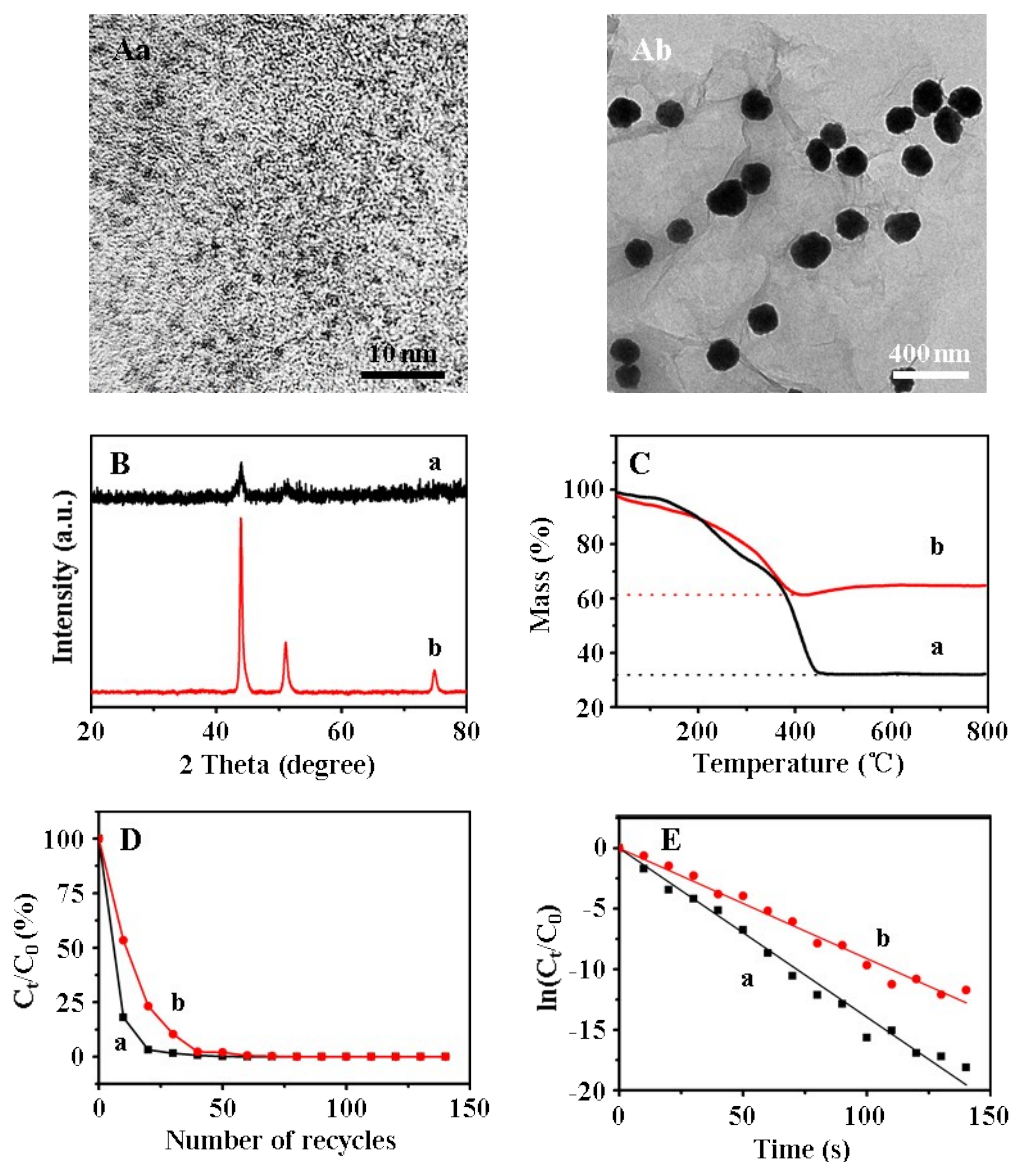
Fig. S9. Graphene/CuNi nanocomposite with different CuNi NPs size((a) ~2 nm, (b) ~200 nm): (A) TEM images; (B) XRD patterns; (C) TG curves; (D) catalytic plots of C_t/C_0; (E) $\ln(C_t/C_0)$ vs time for the reduction of p-nitrophenol.

Fig. S9 gives comparison of the nanocomposite with different CuNi NPs size. The TEM images show the characteristic size of the NPs. In Fig. S9Aa, many small CuNi NPs of sphere shapes with diameter of ~2 nm distributed tightly and evenly on the surface of graphene. From Fig. S9Ab, CuNi NPs with diameter of ~200 nm were observed on the graphene support. The two graphene/CuNi nanocomposite showed characteristic peaks of face center cubic structure of Cu and Ni alloy. The smaller NPs exhibited broader and lower peaks than the larger NPs in XRD pattern in Fig. S9B. Fig. S9C displayed

thermogravity curves of the two graphene/CuNi nanocomposites from room temperature to 800 degree. In the stage before 450 degree, the graphene was oxidized and lead to the weight loss. Meanwhile, the oxidation of the CuNi NPs was taking place. The subsequent weight increase at 500-600 degree revealed the oxidation of the CuNi NPs. The weight increase until temperature reached 700 degree. The nanocomposite with small size CuNi NPs lose ~70% weight but nanocomposite with large size CuNi NPs lose ~40%. The weight loss results revealed the graphene/CuNi nanocomposite with small CuNi NPs size have less amount of metals than the nanocomposite with large CuNi NPs size. Fig. S9D and E show performance of catalytic reduction of p-nitrophenol by the the two nanocomposites. Although the nanocomposite with small CuNi NPs size cost less amount of metals, it received higher activity than the nanocomposite with larger CuNi NPs size. It can be explained that much of the CuNi atoms are at the surface for the nanocomposite with small CuNi NPs size, but atoms of nanocomposite with large CuNi NPs size are much at the internal of the NPs. Therefore, the nanocomposite with small CuNi NPs size have higher activity than the other but cost less metal atoms.
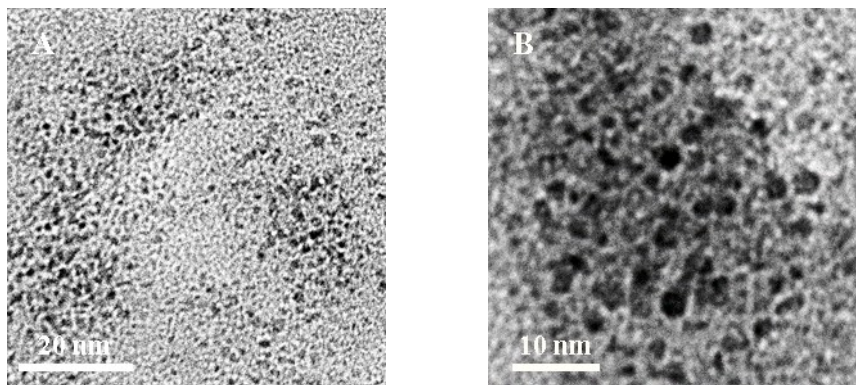
Fig. S10. TEM images in (A) lower and (B) higher magnifications of the graphene/CuNi nanocomposite catalyst retrieved after 25 recycles.

Fig. S10 gives TEM images of the graphene/CuNi nanocomposite catalyst retrieved after 25 catalysis recycles in different magnifications. The images revealed that although underwent 25 catalysis recycles, the CuNi NPs basically kept the original shape and size. It revealed the strong effect of graphene support to prevent the agglomeration of CuNi NPs. The CuNi NPs anchored on graphene strongly, hence protected the activity and lifetime of the catalyst, leading to the superb stability of the catalyst.
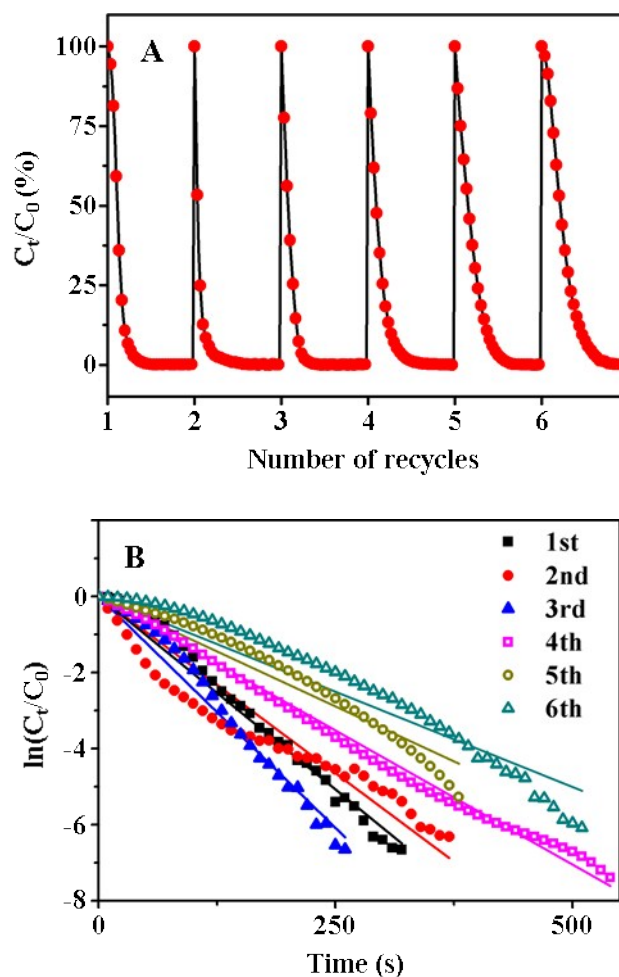
Fig. S11. Lifetime of the CuNi alloy NPs catalyst in the recycles of reduction of p-nitrophenol.

Fig. S11 gives the recycle lifetime of the CuNi alloy NPs catalyst of reduction of p-nitrophenol. From the Fig. S11, it can be seen that the catalyst reached its highest activity in the 3rd recycle, but the activity have not be kept in the following recycles. The reaction rate contant decreased since the 4th recycle and become much lower in the 6th recycle. The data showed the less stability of the alloy NPs catalyst than the graphene/CuNi nanocomposite in lifetime and activiy.
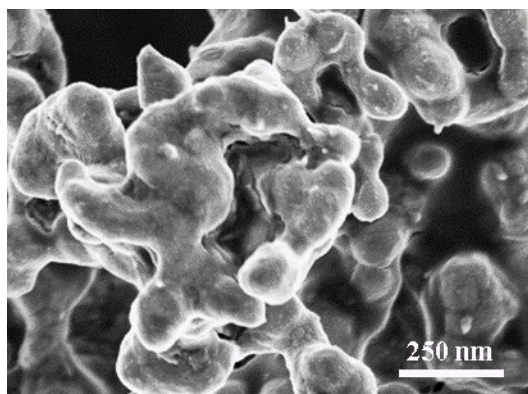
Fig. S12. SEM images of CuNi NPs catalyst after the 6th catalytic recycle.

Fig. S12 gives SEM image of the CuNi NPs catalyst retrieved after 6th catalytic recycle. It is obvious that after 6 catalytic recycles, CuNi NPs have agglomerated together seriously and there was hardly dispersive CuNi NPs. It makes the drastically drop of the surface area compared with the fresh CuNi NPs catalyst, and leads to the fast decrease both in activity and lifetime finally. It can also be demonstrated by the data in Fig. S11.